PCCP

PAPER

View Article Online
View Journal | View Issue

Cite this: *Phys. Chem. Chem. Phys.*, 2018, **20**, 30351

The role of Anderson's rule in determining electronic, optical and transport properties of transition metal dichalcogenide heterostructures†

Ke Xu,[a] Yuanfeng Xu,[a] Hao Zhang, *[a] Bo Peng,[a] Hezhu Shao, *[b] Gang Ni,[a] Jing Li,[a] Mingyuan Yao,[a] Hongliang Lu,[c] Heyuan Zhu*[a] and Costas M. Soukoulis[de]

Received 31st August 2018,
Accepted 12th November 2018

DOI: 10.1039/c8cp05522j

rsc.li/pccp

Two-dimensional (2D) transition metal dichalcogenides (TMDs) MX_2 (M = Mo, W; X = S, Se, Te) possess unique properties and novel applications in optoelectronics, valleytronics and quantum computation. In this work, we performed first-principles calculations to investigate the electronic, optical and transport properties of the van der Waals (vdW) stacked MX_2 heterostructures formed by two individual MX_2 monolayers. We found that the so-called Anderson's rule can effectively classify the band structures of heterostructures into three types: straddling, staggered and broken gap. The broken gap is gapless, while the other two types possess direct (straddling, staggered) or indirect (staggered) band gaps. The indirect band gaps are formed by the relatively higher energy level of Te-d orbitals or the interlayer couplings of M or X atoms. For a large part of the formed MX_2 heterostructures, the conduction band maximum (CBM) and valence band minimum (VBM) reside in two separate monolayers, thus the electron–hole pairs are spatially separated, which may lead to bound excitons with extended lifetimes. The carrier mobilities, which depend on three competitive factors, *i.e.* elastic modulus, effective mass and deformation potential constant, show larger values for electrons of MX_2 heterostructures compared to their constituent monolayers. Finally, the calculated optical properties reveal strong absorption in the ultraviolet region.

1 Introduction

The family of two-dimensional (2D) materials has grown rapidly due to their unique properties, different from their 3D counterparts. A wide range of 2D materials, *e.g.* graphene,[1,2] BN,[3,4] transition metal dichalcogenides (TMDs),[5,6] black phosphorus,[7–9] etc., have been proposed and are under intense investigations. Among these, transition metal dichalcogenides, with the formula MX_2 (where M is a transition metal and X is a chalcogen), are prominent due to their finite direct band gaps with strong optoelectronic responses,[10] large on–off ratios and high carrier mobilities.[11,12] Furthermore, a spin–orbit driven splitting of the valence band was found in 2H monolayer TMDs due to the lack of inversion symmetry, which ultimately allows for valley-selective excitation of carriers.[13–15] In addition, the electronic properties of TMDs can be tuned by strain,[16] multilayers,[17] nanostructuring[18] and electrostatic gating,[19] or by combining individual 2D monolayers into van der Waals (vdW) stacked heterostructures.[20] The vdW heterostructures can be obtained by transfer or direct epitaxial growth.[21,22] The interface of the heterostructures is atomically sharp, with a two-atom thick junction region,[21] and the interlayer coupling intensity can be further tuned. Thus, vdW heterostructures open up many possibilities for creating new TMD material systems with rich functionalities and novel physical properties.[23] When two different atomically thin layers are stacked and bound by van der Waals forces to form MX_2 heterostructures, the electronic properties of the formed vdW MX_2 heterostructures will be significantly affected by the band alignment of the monolayer MX_2, forming various band structures different from the monolayer counterpart, which can be direct- or indirect-band gap, or metallic materials.[24]

[a] *Department of Optical Science and Engineering, Key Laboratory of Micro and Nano Photonic Structures (MoE) and Key Laboratory for Information Science of Electromagnetic Waves (MoE), Fudan University, Shanghai 200433, China. E-mail: zhangh@fudan.edu.cn, hyzhu@fudan.edu.cn*

[b] *Ningbo Institute of Materials Technology and Engineering, Chinese Academy of Sciences, Ningbo 315201, China. E-mail: hzshao@nimte.ac.cn*

[c] *State Key Laboratory of ASIC and System, Institute of Advanced Nanodevices, School of Microelectronics, Fudan University, Shanghai 200433, China*

[d] *Department of Physics and Astronomy and Ames Laboratory, Iowa State University, Ames, Iowa 50011, USA*

[e] *Institute of Electronic Structure and Laser (IESL), FORTH, 71110 Heraklion, Crete, Greece*

† Electronic supplementary information (ESI) available. See DOI: 10.1039/c8cp05522j

Moreover, as we show here, a large proportion of vdW MX_2 heterostructures possess the band structures with the conduction band maximum (CBM) and valence band minimum (VBM) residing in different monolayers. Due to the separate spatial locations of the CBM and VBM, the photon-generated electron–hole pairs are therefore spatially separated, resulting in much longer exciton lifetimes and the possible existence of interlayer exciton condensation,[25] which might help develop two-dimensional lasers, light-emitting diodes and photovoltaic devices.[26,27] The strong interlayer coupling between the two individual MX_2 monolayers in a MoS_2–WSe_2 hetero-bilayer was shown to lead to a new photoluminescence (PL) mode.[28] Hong *et al.* have also investigated the ultrafast charge transfer in a MoS_2–WS_2 heterostructure[29] and found the charge-transfer time is on the femtosecond scale, much smaller than that in monolayer MoS_2 or WS_2. Furthermore, the recombination times of interlayer charge transition are tunable for different stacking orders of MoS_2–WS_2 heterostructures, being 39 ps for the one obtained by vertical epitaxial growth and 1.5 ns for the randomly-stacked bilayer.[30] Finally, tunneling transistors[31] and photovoltaic detectors[32] based on a MoS_2/$MoTe_2$ heterostructure show excellent performance.

Until now, most researches on MX_2 heterostructures focus on S and Se systems. For example, the indirect-to-direct band gap transition and semiconductor-to-metal transition in MoS_2/MX_2(M = Mo, Cr, W, Fe, V; X = S, Se) heterobilayers can be realized by tensile strain or an external electrical field.[33] Heterolayered TMDs (MoS_2, $MoSe_2$, WS_2 and WSe_2) with different stacking modes exhibit tunable direct band gaps.[24] Furthermore, Kang *et al.* calculated the band offsets of MX_2 heterostructures and found that the MoX_2–WX_2 (X = S, Se) heterostructures have type-II band alignment.[34] However, a systematic study on vdW MX_2 heterostructures including a Te system is still lacking. In this paper, using first-principles calculations, we theoretically investigate the electronic, mechanical, transport and optical properties of vdW MX_2 (M = Mo, W; X = S, Se, Te) heterostructures with different stacking modes. The band alignment and interlayer coupling can result in much smaller band gaps of MX_2 heterostructures compared to those of the constituent MX_2 monolayers, and a direct to indirect band gap transition may occur. The excellent mechanical properties show the structural stability of the optimized vdW MX_2 heterostructures. The theoretical values for the transport properties are predicted based on deformation-potential theory. Furthermore, to demonstrate the contribution from monolayer MX_2, the relative relationship between MX_2 heterostructures and the constituent monolayers with respect to the elastic modulus, deformation-potential constants and effective masses is studied in detail. Finally, we also point out the strong optical absorption of the vdW MX_2 heterostructures in the ultraviolet region.

2 Methodology

All calculations are performed using the Vienna *ab initio* simulation package (VASP) based on density functional theory (DFT).[35] The exchange–correlation energy is described by the generalized gradient approximation (GGA) in the Perdew–Burke–Ernzerhof (PBE) parameterization. We choose the DFT-D2/D3 approach to involve the long-distance van der Waals (vdW) interactions.[36–39] The calculation is carried out using the projector-augmented-wave (PAW) pseudopotential method with a plane-wave basis set and a kinetic energy cutoff of 600 eV. A $15 \times 15 \times 1$ Γ-centered k-mesh is used during structural relaxation for the unit cell until the energy differences converge to within 10^{-6} eV, with a Hellman–Feynman force convergence threshold of 10^{-4} eV Å^{-1}. The vacuum size is larger than 25 Å between two adjacent atomic layers to eliminate artificial interactions between them. The electronic band structures of the vdW layered heterostructures are further verified by calculations using a hybrid Heyd–Scuseria–Ernzerhof (HSE06) functional,[40,41] which improves the precision of band structures by reducing the localization and delocalization errors of PBE and Hartree–Fock (HF) functionals. Here, the mixing ratio is 25% for the short-range HF exchange. The screening parameter is 0.2 Å^{-1}.

As we know, electron–phonon scatterings play an important role in determining the intrinsic carrier mobility μ of 2D vdW MX_2 heterostructures, in which the scattering intensities by acoustic phonons are much stronger than those by optic phonons in two-dimensional materials.[42] Therefore, the deformation potential theory for semiconductors, which considers only longitudinal acoustic phonon scattering processes in the long-wavelength limit[43–46] and was originally proposed by Bardeen and Shockley,[47] can be used to calculate the intrinsic carrier mobility of 2D materials. In the long-wavelength limit, the carrier mobility of 2D semiconductors can be written as:[46,48,49]

$$\mu = \frac{2e\hbar^3 C}{3k_B T|m^*|^2 D_l^2}, \quad (1)$$

where e is the electron charge, $\hbar$ is the reduced Planck's constant and T is the temperature (equal to 300 K throughout the paper). C is the elastic modulus of a uniformly deformed crystal by strain and derived from $C = [\partial^2 E/\partial^2(\Delta l/l_0)]/S_0$, in which E is the total energy, Δl represents the change of lattice constant l_0 along the strain direction and S_0 is the lattice area at equilibrium for a 2D system. m^* is the effective mass given by $m^* = \hbar^2(\partial^2 E(k)/\partial k^2)^{-1}$ (k is wave-vector, and $E(k)$ is the energy). The spacing of the k-mesh we used to calculate the effective masses is 0.02 [Å^{-1}]. In addition, D_l is the deformation potential (DP) constant defined by $D_l^{e(h)} = \Delta E_{CBM(VBM)}/(\Delta l/l_0)$, where $\Delta E_{CBM(VBM)}$ is the energy shift of the band edge with respect to the vacuum level under a small dilation Δl of the lattice constant l_0.

3 Results and discussion

3.1 Geometric structures of hetero-bilayer MX_2

Generally, MX_2 crystals have four stable lattice structures, *i.e.*, 2H, 1T, 1T′ and 3R,[50] with the first being the dominant one in nature at room temperature. Most MX_2 crystals, like MoS_2 and WSe_2 with a stable 2H phase (1H for monolayer),

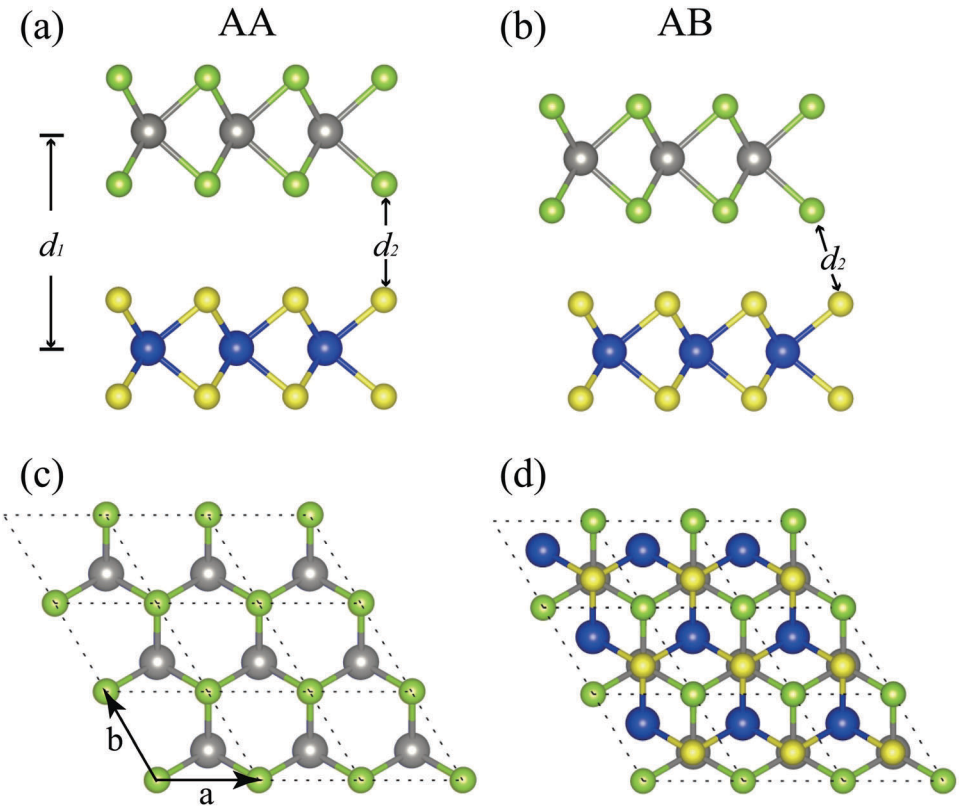

Fig. 1 Atomic structure of AA stacking and AB stacking hetero-bilayer MX_2 in a 3 × 3 × 1 supercell from a side view (upper panel) and top view (lower panel), respectively. Large and small spheres represent the M and X atoms, respectively. Color coding is used to distinguish the different atomic species. d_1 and d_2 are the interlayer distance (M_1–M_2) and the bond length of X_1–X_2, respectively.

have been studied widely.[51] For 2H-phase MX_2 crystals, the M atoms and X atoms are located in different layers, which can be described by the point group D_{3h}. While for the 3R-phase unit cell shown as Fig. 1(b and d), one M atom is eclipsed by the X atoms above and the other one is located in the hexagonal center, leading to the AB Bernal stacking. In fact, the electronic structure of the MX_2 heterostructure is sensitive to the stacking modes, due to the different interlayer interactions. AA and AB stacking structures possess the weakest and strongest interlayer electronic coupling, respectively.[52] For simplicity, we only consider these two stacking modes. However, some interesting properties, *e.g.* the relatively constant change in both electronic and mechanical couplings at twist angles between 0° (AA stacking) and 60° (AB stacking) found in twisted MoS_2 bilayers[53] and so on, may not be captured by these two modes and are beyond the scope of our work. One stacking type can be geometrically transformed to the other by horizontal sliding or by rotation around the vertical axis. For MX_2 heterostructures with two different constituent monolayer MX_2 crystals, both AA and AB stacking crystals possess a lower symmetry of C_{3v} point group, with the symmetry operations of C_3 and vertical mirror reflection σ_v[54] rather than the mirror reflection operation σ_h in the horizontal plane.

To determine the energetically stable structure before geometry optimization, an interlayer-distance optimization algorithm is implemented to reach an optimized d_1 (defined in Fig. 1(a)) using the universal binding energy relation (UBER) method, which provides a simple universal form for the relationship between binding energy and atomic separation.[55,56] The optimized interlayer distance is predicted from a series of unrelaxed models with different values of d_1 (from 5 to 8 Å). We then calculate the surface adhesion energy W_{ad} for all 30 types of 2D vdW MX_2 heterostructure under investigation here (*e.g.* MoS_2/WSe_2 hetero-bilayer),

$$W_{ad} = \frac{E_{MoS_2} + E_{WSe_2} - E_{MoS_2/WSe_2}}{A}, \quad (2)$$

where A is the interface area and E_{MoS_2}, E_{WSe_2} and E_{MoS_2/WSe_2} are the total energies of the monolayer MoS_2 and WSe_2 and the MoS_2/Wse[2] heterostructure, respectively. The optimal interlayer distances d_1 can be obtained by maximizing the value of W_{ad}. Then, further structure optimizations are implemented without any external constraints. Furthermore, the formation energies E ($E = E_{AB} - E_A - E_B$) are listed in Table S2 (ESI†). The negative values for the formation energies also confirm the stability of our structures and, for most MX_2 heterostructures, AA stacking is more energetically favorable.

The calculated lattice constants a and interlayer distances d for the above-mentioned 30 types of 2D MX_2 heterostructure are summarized in Table 1 and are in good agreement with previous theoretical and experimental results.[57–60] As shown in Table 1, the optimized interlayer distances of AA stacking structures are larger than those of the corresponding AB

Table 1 Hetero-bilayer system and band alignment type, optimized lattice constant a (Å), interlayer distance d_1 (Å), the atomic distance d_2 (Å) between the adjacent anion in different layers and the band gap of MX_2 heterostructures (PBE/HSE/SOC). Other theoretical data are also listed in parentheses for comparison

System (Anderson)	Stacking type	a (Å)	d_1 (Å)	d_2 (Å)	Band type	$E_g^{PBE}/E_g^{HSE}/E_g^{SOC}$ (eV)
MoS_2–WSe_2(II)	AA	3.214 (3.22[61])	6.828	3.573	Direct	0.60(0.57[62])/1.19/0.37
	AB	3.215	6.164	3.455	Direct	0.75/1.33/0.53
MoS_2–WS_2(II)	AA	3.183 (3.18[57])	6.758 (6.8[58])	4.826	Indirect	1.29(1.16[62])/1.93/1.22
	AB	3.187	6.137 (6.3[58])	3.535	Indirect	1.08/1.70/1.06
WS_2–WSe_2(II)	AA	3.213 (3.204[24])	6.864	4.808	Direct	0.93(1.007[24])/1.43/0.67
	AB	3.212	6.229	3.503	Direct	1.05/1.56/0.80
$MoSe_2$–WS_2(II)	AA	3.211 (3.210[24])	6.877	4.820	Direct	1.13 (1.154[24])/1.53/1.00
	AB	3.212	6.295	3.570	Direct	1.09 /1.48/0.97
$MoSe_2$–WSe_2(II)	AA	3.279 (3.277[24])	7.019 (6.62[59])	4.913	Indirect	1.30 (1.330[24])/1.86/1.03
	AB	3.279	6.362(6.48[59])	3.554	Indirect	1.28/1.77/1.09
MoS_2–$MoSe_2$(II)	AA	3.250 (3.26[62])	6.972	4.940	Direct	0.98(0.74[62])/1.10/0.56
	AB	3.254	6.350	3.655	Direct	0.65/1.09/0.56
$MoTe_2$–MoS_2(II)	AA	3.328	7.267	5.058	—	—/0.45/—
	AB	3.347	6.575	3.736	—	—/0.47/—
$MoTe_2$–$MoSe_2$(II)	AA	3.413	7.421	5.177	Indirect	0.49/0.95/0.19
	AB	3.413	6.784	3.853	Indirect	0.51/0.95/0.21
$MoTe_2$–WS_2(II)	AA	3.347	7.170	4.984	—	—/0.43/—
	AB	3.350	6.576	3.757	—	—/0.42/—
$MoTe_2$–WSe_2(I)	AA	3.425	7.354	5.136	Indirect	0.69/1.05/0.60
	AB	3.423	6.725	3.811	Indirect	0.64/1.00/0.53
$MoTe_2$–WTe_2(II)	AA	3.538(3.56[60])	7.646	5.348	Direct	0.95/1.44/0.67
	AB	3.543	6.954	3.923	Indirect	0.93/1.46/0.74
WTe_2–MoS_2(III)	AA	3.354	7.204	5.018	—	—/0.46/—
	AB	3.358	6.584	3.751	—	—/0.37/—
WTe_2–$MoSe_2$(II)	AA	3.423	7.358	5.128	Direct	0.33/0.85/0.10
	AB	3.429	6.740	3.833	Direct	0.35/0.84/0.11
WTe_2–WS_2(III)	AA	3.360	7.114	4.963	—	—/0.41/—
	AB	3.365	6.516	3.717	—	—/0.40/—
WTe_2–WSe_2(I)	AA	3.422	7.288	5.092	Direct	0.51/0.93/0.24
	AB	3.447	6.679	3.781	Direct	0.45/0.86/0.17

stacking structures. This is due to the fact that, in AB structures, the X atoms are not aligned along the vertical axis and a shorter interlayer distance leads to a smaller total energy. Furthermore, the change of stacking type of the heterostructures will affect the interlayer interactions of M or X atoms.

3.2 Electronic band structure of hetero-bilayer MX_2

Previous studies have revealed that monolayer MX_2 possesses a direct band gap and both the CBM and VBM are located at the K point in the first Brillouin zone.[17,34,63,64] Owing to the lack of inversion symmetry and the strong spin–orbit coupling (SOC), the valence bands possess a significant spin–orbit splitting at the K valleys.[65] The band alignment for MX_2 shows the following trends (see Fig. 2(b)): (1) for common-X systems, the band gaps of MoX_2 are larger than that of WX_2, and the CBM and VBM of WX_2 are higher than those of MoX_2; (2) for common-M systems, an increase in the atomic number of X results in a shallower anion p orbital and thus a shift of the VBM to higher

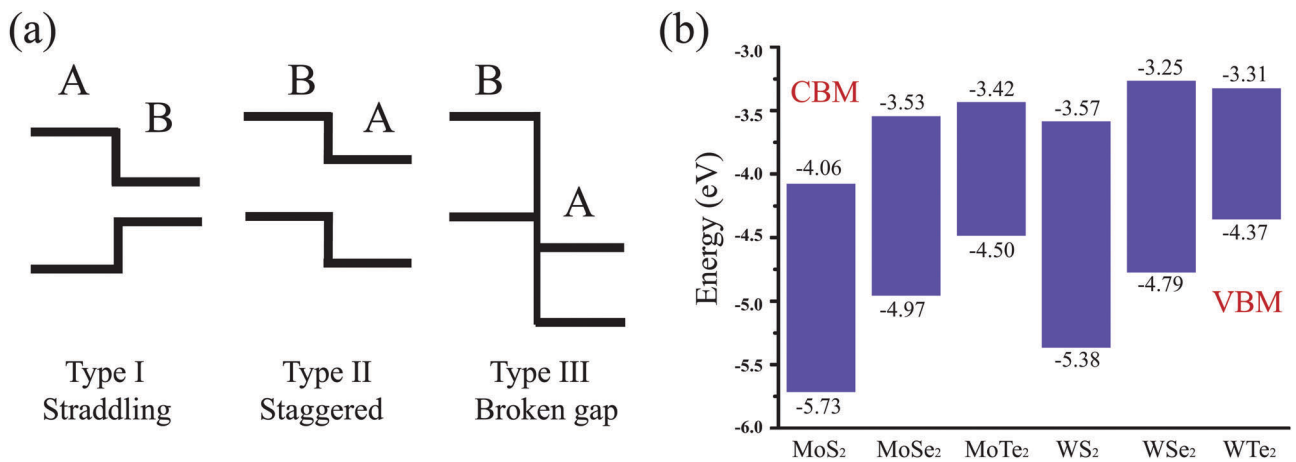

Fig. 2 (a) Various possible band-edge lineups in semiconductors A and B. (b) Band alignment for monolayer MX_2. The vacuum level is taken as 0 reference.

energy levels, finally leading to decreased band gaps.[66] To understand these two trends in band alignment, the atomic orbital composition of the states should be taken into consideration. Taking MoS_2 as an example, the CBM of MoS_2 is mainly composed of the d_{z^2} orbital of Mo and the p_x and p_y orbitals of S, whereas the VBM mostly consists of the $d_{x^2-y^2}$ and d_{xy} orbitals of Mo.

For the hetero-bilayer MX_2 crystals constructed from two MX_2 monolayers, the formation of their band structures can be understood by the so-called Anderson's rule, which provides a scheme for the construction of energy band diagrams for heterostructures consisting of two semiconductor materials.[67] According to Anderson's rule, the vacuum energy levels of the two constituent semiconductors on either side of the heterostructure should be aligned at the same energy,[68] and there are three types of possible band-edge lineups: straddling, staggered and broken gap, as shown in Fig. 2(a). For type I heterostructures, the CBM and VBM mainly consist of the orbitals of semiconductor B, which possesses a smaller band gap compared to semiconductor A. Thus, the band type of the heterostructure is consistent with the smaller-gap material. For type II heterostructures, the VBM and CBM around the Fermi

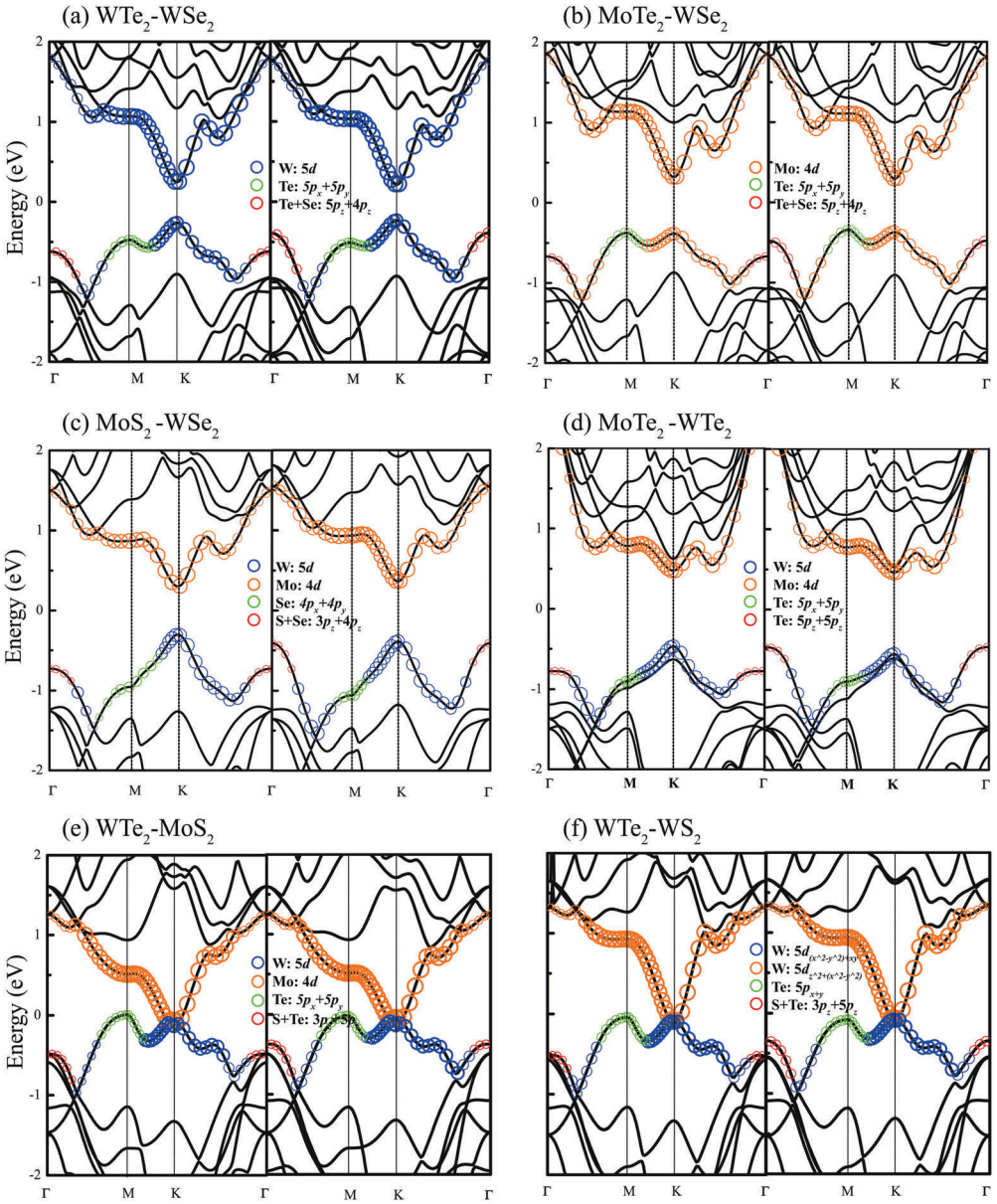

Fig. 3 Band structures of the AA and AB stacking vdW MX_2 heterostructures and atomic orbital weights in the energy bands. The blue and orange circles represent d orbitals of the cations. The green and red circles represent p_x + p_y and p_z orbitals of the anions, respectively. The size of each circle is proportional to the weight of the atomic orbital. (a and b) Type I band alignment system: WTe_2–WSe_2 and $MoTe_2$–WSe_2 hetero-bilayer. (c and d) Type II band alignment system: MoS_2–WSe_2 and $MoSe_2$–WSe_2 hetero-bilayer. (e and f) Type III band alignment system: WTe_2–MoS_2 and WTe_2–WS_2 hetero-bilayer.

level reside in two separate semiconductors, and the formed heterostructure still possesses a small direct or indirect band gap. As for type III heterostructures, the locations of the CBM and VBM are similar to those of type II heterostructures, but band gap does not exist, and the formed heterostructure is a semi-metal. It should be noted that, for type II and type III heterostructures, since the CBM and VBM may locate in different semiconductors, the photon-generated excitons are thus spatially separated, which will suppress the recombination of electron–hole pairs and extend the exciton lifetime compared with the corresponding individual semiconductors.[26,27,34,69–71]

The band structures for the vdW MX_2 heterostructures are calculated using the PBE and HSE06 method and the results, *i.e.*, band types and band gaps, are shown in Table 1. The direct band gap at the *K* point for monolayer MX_2 is transformed into three types of band gap when a hetero-bilayer MX_2 crystal is formed, *i.e.*, direct, indirect (*M*–*K*, *Γ*–*K*, *K*–*Q*) and zero band gap or overlapping bands, according to the calculated results shown in Table 1 and the above-mentioned analyses based on Anderson's rule. The formation types of band gap for the vdW MX_2 heterostructures categorized according to Anderson's rule are also shown in Table 1. The classification of the band types according to Anderson's rule is called as Anderson band type hereafter. It is shown in Table 1 that the Anderson band types for the vdW MX_2 are determined by the constituent monolayer MX_2 irrespective of the stacking manner. This is probably due to the fact that the VBM/CBM of the hetero-bilayer structure is attributed to the d/p-orbitals of M/X atoms, and the weak vdW interactions will not change the charge distribution of the constituent monolayers significantly, thus the relative CBM/VBM energies of the constituent monolayers will not change.

For simplicity, we first consider the Anderson band type I heterostructure, *e.g.* band structures for WTe_2–WSe_2 and $MoTe_2$–WSe_2 hetero-bilayers, shown in Fig. 3(a and b). Generally, as we mentioned above, two monolayer MX_2 crystals with identical M atoms but different X atoms possess different CBM/VBM energy levels, and the crystal with the X atoms with the larger atomic number has a higher energy level CBM or VBM. However, as shown in Fig. 2(b), the CBM energy level of WTe_2 is lower than that of WSe_2, although the atomic number of Te is larger than Se. Such a deviation can be understood by the fact that the bond length $d_{W–Te}$ of WTe_2 is the largest one among those of the monolayer MX_2 crystals, which leads to a small overlap integral *V* between the d orbitals of the M atoms and the p orbitals of the X atoms for the formation of the CBM due to $V \propto 1/d_{W–Te}^2$,[72,73] and thus counteracts the increase of the CBM energy level from Se with smaller p orbitals compared to Te.[34] The smaller CBM energy level of WTe_2 ultimately results in the Anderson band type-I alignment of band edges in the WTe_2–WSe_2 hetero-bilayer, leading to a direct band gap at the *K* point for both AA and AB stacking manners, as shown in Fig. 3(a).

According to Table 1, most of the hetero-bilayer MX_2 crystals are Anderson band type II heterostructures, *e.g.*, hetero-bilayer MoS_2–WSe_2 and $MoTe_2$–WTe_2. Fig. 3(c) shows the energy band structures of the AA and AB stacking MoS_2–WSe_2 hetero-bilayers, exhibiting direct band gaps of 0.60 eV and 0.75 eV for the AA and AB stacking types, respectively, which are consistent with the previous results.[33] The CBM locates in the MoS_2 layer and the VBM locates in the WSe_2 layer, resulting in the formation of spatially separated electron–hole pairs. Experiments on hetero-bilayer MoS_2–WSe_2 revealed the dramatic quenching of the photoluminescence (PL) intensities[28] and the extended exciton lifetime.[27]

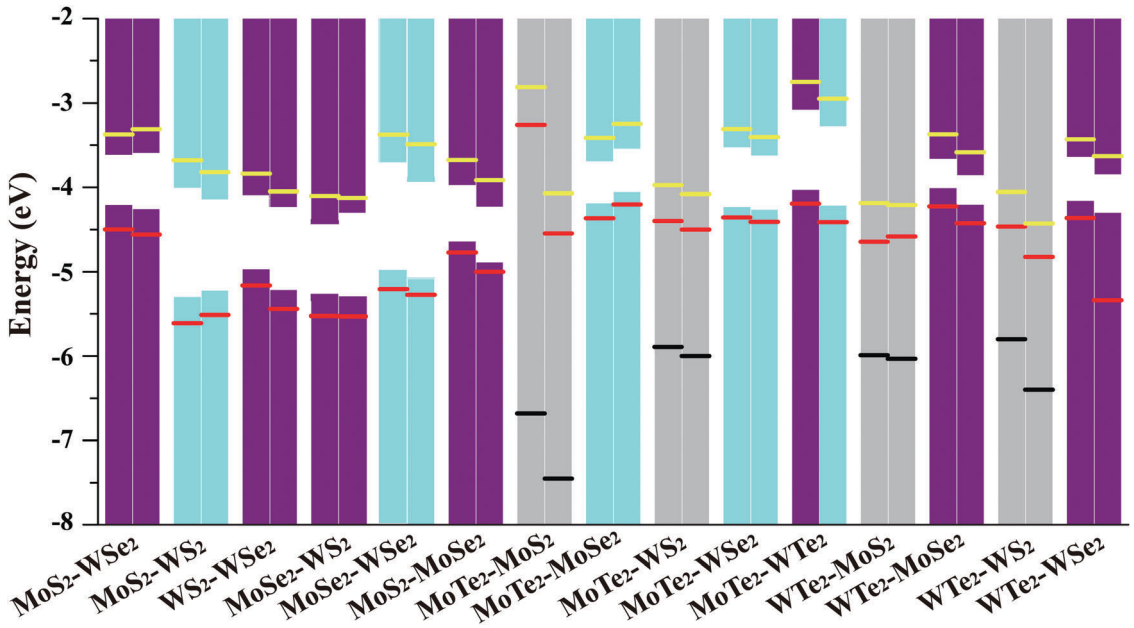

Fig. 4 Calculated band alignment for the vdW MX_2 heterostructures. The histogram is obtained by PBE, with the purple, blue and grey representing the direct band gap, indirect band gap and zero-band gap, respectively. The red and yellow solid lines represent the VBM and the CBM obtained by HSE.

As for the formation of indirect band gaps for type-II heterostructures, there are three types of such indirect band gap, *i.e. M–K*, *Γ–K* and *K–Q*, resulting from the relatively higher energy level of the Te-5p orbital, the relatively stronger p_z–p_z bonds of X atoms in different monolayers and the hybridization of M-d and X-p orbitals, respectively.

As shown in Fig. 3, the valence band at the *M* point is attributed to the p_x and p_y orbitals of X atoms, and the corresponding energy level for hetero-bilayer MX_2 crystals containing Te atoms is larger than those only containing Se or S atoms, since the atomic number of Te is the largest one. Therefore, for hetero-bilayer MTe_2–MX_2, the valence band energies at the *M* point significantly increase compared with the hetero-bilayer MSe_2–MX_2 (X ≠ Te) or MS_2–MX_2 (X ≠ Te), which subsequently leads to the formation of the *M–K* indirect band gap, *e.g.* hetero-bilayer $MoTe_2$–WSe_2, as shown in Fig. 3(b).

The valence band at the *Γ* point can be attributed to the inter-layer overlap integral of p_z orbitals of X atoms belonging to different monolayers at the *Γ* point, as shown in Fig. 3. For hetero-bilayer MX_2 considered here, the distance between X atoms in different monolayers for the AB stacking hetero-bilayer, *i.e.* d_2 shown in Fig. 1(a and b), is smaller than the corresponding AA stacking hetero-bilayer, as shown in Table 1, thus the energy level of the valence band at the *Γ* point for the former is the higher one, due to $V_{p_z-p_z} \propto 1/{d_2}^2$. The increase of the energy level of the valence band at *Γ* points sometimes leads to the formation of *Γ–K* indirect band gaps with AB stacking, *e.g.* AB-stacking $MoTe_2$–WTe_2 as shown in Fig. 3(d).

Another indirect band gap (*K–Q*), *e.g.* $MoSe_2$–WSe_2 shown in Fig. S2 (ESI†), is formed by the VBM located at the *K* point and the CBM located at the *Q* point between *Γ* and *K*. According to the analysis on the atomic orbitals, the energy level of the valence band at the *Q* point is formed by the strong hybridization between the Mo-d orbitals and W-d orbitals, which lowers the energy level at the *Q* point and ultimately leads to the shift of the CBM from the *K* to *Q* point.[74] However, the CBM and VBM at *K* are insignificantly hybridized, due to the higher symmetry and a larger bond length d_{Mo-W} compared to those at the *Q* point,[57] thus the VBM is fixed at the *K* point.

The extreme state of staggering is the formation of broken band gaps, which is also known as the Anderson band type III alignment, as shown in Fig. 2(a). For example, the CBMs of MoS_2 and WS_2 are much lower than those of other MX_2 monolayers and WTe_2 possesses the highest VBM, as shown in Fig. 2(b). The band alignment in hetero-bilayer WTe_2–MoS_2 and WTe_2–WS_2 thus can be approximately considered as the Anderson band type III alignment, as shown in Fig. 3(e and f). The band overlaps at the *K* point, changing the heterostructures into metallic phase.

The band gaps of the hetero-bilayer MX_2 crystals based on the HSE06 and SOC calculations are also provided in Table 1 and Fig. 4. The negative SOC effects decrease the band gap and the HSE calculations increase the band gap by 0.4–0.6 eV, compared to the PBE calculations. It should be noted that the metallic phases of the hetero-bilayer MX_2 crystals, *i.e.* the Anderson band type III heterostructures, *e.g.* hetero-bilayer WTe_2–MoS_2 and WTe_2–WS_2 crystals as shown in Fig. 3(e and f), are replaced by direct band gaps based on HSE calculations, which means that the hetero-bilayer MX_2 crystals considered here do not possess Anderson band type III alignment.

In summary, the CBM state at the *K* point is weakly localized and not usually affected by the stacking types. The VBM may shift from the *K* to *Γ* point in regard to different stacking types due to the interlayer electronic coupling. Kang *et al.* have stated that the interlayer coupling strength of the AB configuration at the *Γ* point is the strongest among the heterostructures with arbitrary in-plane angular rotations to push the band energy at the *Γ* point up to a highest level.[75] In contrast, the interlayer coupling strength of AA configuration (0 degree) is the weakest. This argument can be proved by the Moiré pattern of these heterostructures to demonstrate that the pattern becomes smaller and more complex with the rotation angle θ increasing. Moreover, this Moiré pattern-induced wave function localization of the VBM will significantly affect the carrier mobilities of MX_2 heterostructures and will be discussed in the next section.

3.3 Mechanical properties and transport properties of hetero-bilayer MX_2

Since the MX_2 heterostructures under consideration here possess C_{3v} symmetry, the number of independent second-order elastic coefficients c_{ij} is five and $c_{11} = c_{22}$.[76] The calculated elastic coefficients of all MX_2 heterostructures are shown in Table S2 (ESI†) and all the vdW MX_2 heterostructures are mechanically stable, according to the Born criteria:[77]

$$C_{11} - C_{12} > 0,\ C_{11} + 2C_{12} > 0,\ C_{44} > 0 \qquad (3)$$

The 2D Young's moduli of all MX_2 heterostructures, given by $Y^{2D} = \frac{c_{11}c_{22} - {c_{12}}^2}{c_{11}}$,[78] are listed in Table 2. The 2D Young's modulus for monolayer MX_2 crystals decreases from MS_2 to MSe_2 to MTe_2,[79] which is due to the fact that the strength of $d_{xy,yz,zx}$–p orbital coupling, which forms M–X bonding, becomes weaker with an increase of the atomic number of chalcogen.[80] The calculated 2D Young's moduli for monolayer MX_2 crystals are shown in Table S1 (ESI†). The contributions to the mechanical properties of MX_2 heterostructures can be roughly considered from constituent monolayer MX_2 crystals and the weak interlayer bonding.

The Young's moduli of the MTe_2–MX_2 heterostructures are lower than others due to the weakest Y^{2D} of monolayer MTe_2 among the monolayer MX_2 crystals considered here. Meanwhile, the Young's moduli of the MX_2 heterostructures are a little lower than the sum of those of the constituent monolayer MX_2 crystals, which means that the contribution from the interlayer bonding to the total Young's modulus is negative. The Poisson's ratio is given by $v^{2D} = \frac{c_{12}}{c_{22}}$,[78] which describes the lateral deformation when applying uniaxial strains, is calculated and shown in Table 2. Generally materials with a high Poisson's ratio possess good plasticity. The Poisson's ratios for the MX_2 heterostructures are numerically close to each other except WTe_2–MX_2, with the lowest Poisson's ratio

Table 2 Hetero-bilayer system and band alignment type, Young's modulus Y (GPa), Poisson's ratio v, electron and hole effective masses along the armchair direction, deformation potential constants for CBM and VBM, elastic modulus and electron and hole mobilities along armchair direction. System (Anderson)

System (Anderson)	Stacking type	Y (N m^{-1})	v	m_e^* (m_0)	m_h^* (m_0)	D_l^e	D_l^h	C (N m^{-1})	μ_e (cm^2 (V s)$^{-1}$)	μ_h (cm^2 (V s)$^{-1}$)
MoS_2–WSe_2(II)	AA	217.58	0.25	0.47	0.47	3.05	3.26	139.55	961.16	875.94
	AB	211.03	0.27	0.48	0.46	4.05	2.43	152.92	573.03	1808.89
MoS_2–WS_2(II)	AA	241.46	0.25	0.46	1.70	6.01	5.70	127.81	256.46	18.04
	AB	242.03	0.24	0.46	0.92	6.28	5.03	121.19	318.08	76.70
WS_2–WSe_2(II)	AA	229.08	0.26	0.30	0.47	3.44	3.60	149.27	1990.11	770.94
	AB	226.75	0.26	0.26	0.45	4.85	2.38	151.14	1345.29	1947.10
$MoSe_2$–WS_2(II)	AA	261.16	0.31	0.28	0.62	3.26	3.38	152.12	2575.74	511.18
	AB	272.66	0.32	0.29	0.58	5.09	1.87	92.47	600.18	1158.73
$MoSe_2$–WSe_2(II)	AA	218.88	0.27	0.67	0.45	4.29	1.59	130.84	224.10	3752.36
	AB	212.42	0.28	0.61	1.12	1.93	2.84	122.16	1239.06	177.56
MoS_2–$MoSe_2$(II)	AA	232.78	0.26	0.42	0.71	2.87	2.78	125.83	1321.55	454.69
	AB	230.26	0.27	0.42	0.71	3.07	4.50	114.86	758.03	359.04
$MoTe_2$–MoS_2(II)	AA	196.82	0.36							
	AB	196.87	0.34							
$MoTe_2$–$MoSe_2$(II)	AA	184.77	0.31	0.46	1.37	4.40	3.74	113.18	532.75	45.79
	AB	200.46	0.25	0.46	1.37	4.07	3.75	110.81	532.75	45.79
$MoTe_2$–WS_2(II)	AA	206.17	0.28							
	AB	195.86	0.31							
$MoTe_2$–WSe_2(I)	AA	183.70	0.28	0.30	1.33	3.95	3.83	109.1	515.87	52.52
	AB	194.71	0.24	0.30	1.25	4.41	4.14	114.79	1191.02	58.76
$MoTe_2$–WTe_2(II)	AA	136.33	0.39	0.57	0.42	1.61	1.38	101.62	1023.61	55.76
	AB	171.83	0.22	0.58	3.46	4.32	3.30	99.43	2315.94	3285.72
WTe_2–MoS_2(III)	AA	169.33	0.20							
	AB	189.09	0.28							
WTe_2–$MoSe_2$(II)	AA	183.83	0.27	0.45	0.48	2.65	2.85	109.47	382.87	6.58
	AB	196.41	0.22	0.45	0.48	2.70	2.85	102.26	912.5	987.31
WTe_2–WS_2(III)	AA	189.00	0.20							
	AB	233.27	0.29							
WTe_2–WSe_2(I)	AA	168.36	0.33	0.30	0.46	2.95	2.97	113.4	912.5	987.31
	AB	197.77	0.22	0.30	0.45	2.79	3.08	115.65	875.3	918.66

of 0.20 of monolayer WTe_2 crystal among the monolayer MX_2 crystals (see Table S1, ESI†).

The effective masses for electrons m_e^* and holes m_h^* of vdW MX_2 heterostructures along armchair and zigzag directions are calculated, and the results along the armchair direction are shown in Table 2. The values of m_e^* for AA-stacking MX_2 heterostructures are close to those of the corresponding AB-stacking ones, however, the values of m_h^* for AA-stacking heterostructures are obviously deviated from those of AB-stacking ones, *e.g.* MoS_2–WS_2 and $MoTe_2$–WTe_2 heterostructures, especially when the band types for AA and AB stackings are different (direct *vs.* indirect), as shown in Tables 1 and 2. Such phenomena can be understood by the fixed CBM (electrons) at the K or Q point for all the MX_2 heterostructures, and the transition of the VBM (holes) from the K point to the M or Γ point for MX_2 heterostructures with an indirect band gap.

As mentioned above, the band structures of MX_2 heterostructures can be roughly decomposed into those of the constituent monolayer MX_2 crystals, according to Anderson's rule, which also leads to the formation of the effective masses of electrons and holes for MX_2 heterostructures. Fig. 5 shows the effective masses of electrons and holes for MX_2 heterostructures and the corresponding constituent monolayer MX_2 crystals along all directions, taking WTe_2–WSe_2 and MoS_2–WSe_2 hetero-bilayer as examples without loss of generality.

The WTe_2–WSe_2 hetero-bilayer belongs to Anderson band type I and the CBM and VBM are attributed to those of the monolayer WTe_2 crystal. It is shown in Fig. 5(a and b) that the effective masses of electrons and holes for the WTe_2–WSe_2 hetero-bilayer are close to those of monolayer WTe_2 crystals. However, for MoS_2–WSe_2 hetero-bilayers (Anderson band type II), since the CBM is attributed to that of monolayer MoS_2 crystals and the VBM is attributed to that of monolayer WSe_2 crystals, the m_e^* value for the MoS_2–WSe_2 hetero-bilayer is similar to that of monolayer MoS_2 and the m_h^* value is similar to that of monolayer WSe_2, as shown in Fig. 5(c and d).

According to eqn (1), the third factor determining carrier mobilities μ is the deformation potential constant, $D_l^{e,h}$, which describes the scatterings of electrons/holes by longitudinal acoustic phonons. The calculated $D_l^{e,h}$ values for MX_2 heterostructures and monolayer MX_2 crystals are shown in Table 2 and Table S1 (ESI†), respectively. By comparison, it is found that the deformation potential constants of MX_2 heterostructures are larger overall than those of the constituent monolayer MX_2, which means that the formation of the vdW MX_2 heterostructures increases the electron–acoustic phonon coupling, leading to the increase of deformation potential constant D_l, especially for MoS_2–WS_2 heterostructures.

Since the CBM and VBM of the MX_2 heterostructures can be attributed to the respective band structures of the constituent monolayer MX_2, according to the Anderson rule, the shift of the VBM from the K point to the Γ/M point will result in a dramatic change of the deformation potential constants and hole effective masses for MX_2 heterostructures with indirect band gaps, *e.g.* $MoTe_2$–WTe_2.

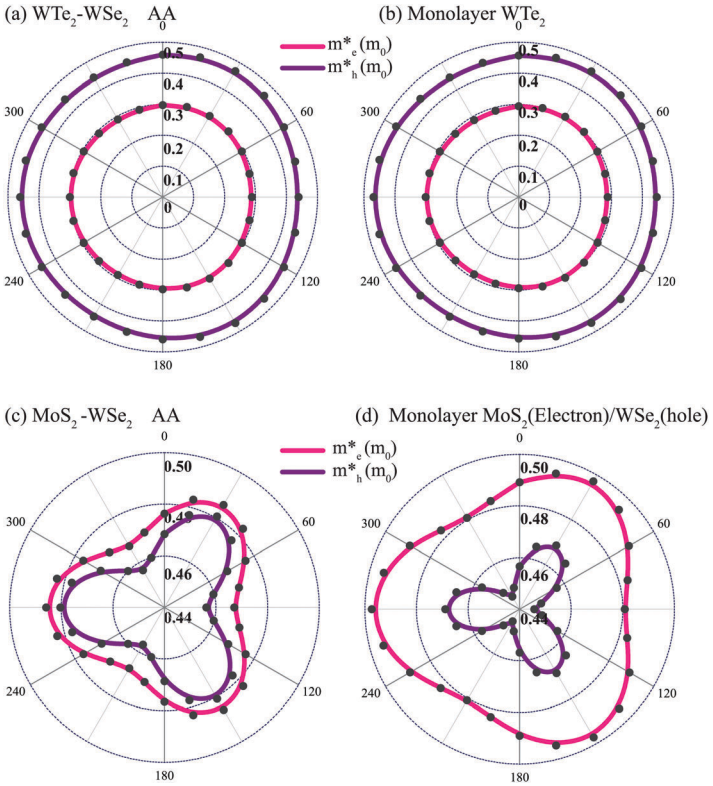

Fig. 5 The calculated carrier (hole mass$_h$* and electron mass$_e$*) for (a) type I band alignment system (WTe_2–WSe_2 hetero-bilayer), (b) monolayer WTe_2, (c) type II band alignment system (MoS_2–WSe_2 hetero-bilayer) and (d) monolayer MoS_2 (electron) and WSe_2 (hole).

In order to figure out the exact contributions from the three factors, *i.e.* effective masses $m_{e,h}$*, deformation potential constants $D_l^{e,h}$ and elastic modulus C, to the carrier mobilities μ, compared to the constituent monolayer MX_2 crystals, we plot the values of the three factors for constituent monolayer crystals and hetero-bilayer structures in Fig. S4 (ESI†). It is clear that the elastic modulus of hetero-bilayer structures is nearly twice that of the constituent monolayer MX_2 crystals, while the deformation potential constants of hetero-bilayer structures are larger overall or close to the constituent monolayer MX_2 crystals. Moreover, the effective masses of hetero-bilayer structures, mostly determined by the constituent monolayer crystals, are close to those of the constituent monolayer crystals, except some hetero-bilayer structures with VBM points shifted from K to Γ/M, *e.g.* $MoTe_2$–WTe_2. Finally, the carrier mobility of electrons and holes along armchair and zigzag directions for the MX_2 hetero-bilayer can be calculated according to eqn (1), as shown in Fig. 6. Fig. 6(a, b) and (c, d) show electron/hole mobilities along armchair and zigzag directions, respectively. The mobilities for monolayer MX_2 as a contrast are shown as color blocks in the diagonal direction and the color blocks in the lower/upper triangular part correspond to the cases of AA/AB-stacking types. For example, the red block of the 1st row and 4th column in Fig. 6(a) corresponds to the electron mobilities along the armchair direction of the AB-stacking MoS_2–WSe_2 heterostructure, *i.e.* $\mu = 573\ cm^2\ (V\ s)^{-1}$. The electron mobilities of hetero-bilayer structures are larger overall than those of constituent monolayer MX_2 crystals, and the same situation takes place for the hole mobilities of hetero-bilayer structures with the VBM located at the K point. However, the hole mobilities of hetero-bilayer structures with the VBM located at the Γ/M point are smaller than those of constituent monolayer MX_2 crystals.

The AA stacked $MoTe_2$–$MoSe_2$ heterostructure possesses the highest electron mobility along the zigzag direction, *i.e.* $3658\ cm^2\ (V\ s)^{-1}$, and the AA stacked $MoSe_2$–WSe_2 heterostructure possesses the highest hole mobility along the armchair direction, *i.e.* $3752\ cm^2\ (V\ s)^{-1}$.

3.4 Optical properties of hetero-bilayer MX_2

The optical properties of the vdW MX_2 heterostructures are described by the complex dielectric function, *i.e.* $\varepsilon(\omega) = \varepsilon_1(\omega) + i\varepsilon_2(\omega)$. The imaginary part of the dielectric tensor $\varepsilon_2(\omega)$ is determined by a summation over empty band states as follows:[81,82]

$$\varepsilon_2(\omega) = \frac{2\pi e^2}{\Omega\varepsilon_0}\sum_{k,v,c}\delta\left(E_k^c - E_k^v - \hbar\omega\right)\left|\left\langle\Psi_k^c\middle|\mathbf{u}\cdot\mathbf{r}\middle|\Psi_k^v\right\rangle\right|^2, \qquad (4)$$

where Ω is the crystal volume, ε_0 is the vacuum dielectric constant, $\hbar\omega$ represents the photon energy, v and c mean the valence and conduction bands respectively, $\mathbf{u}$ is the polarization vector in the incident electric field, $\mathbf{u}\cdot\mathbf{r}$ is the momentum operator and Ψ_k is the wave function at the k point. The real

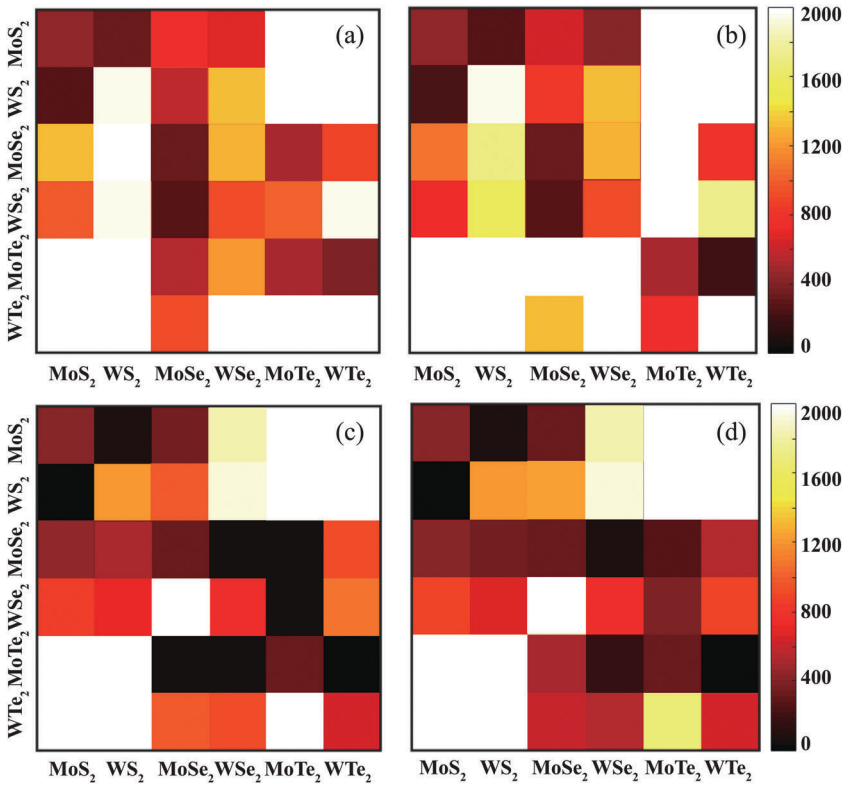

Fig. 6 The calculated carrier mobilities for the vdW MX_2 heterostructures, with the AA stackings in the lower left corner and AB stackings in the upper right corner. The values along the diagonal are the mobilities for monolayer MX_2.(a and b) The electron mobilities of the vdW MX_2 heterostructures along armchair and zigzag directions, respectively; (c and d) The hole mobilities of the vdW MX_2 heterostructures along armchair and zigzag directions, respectively.

part of the dielectric tensor $\varepsilon_1(\omega)$ is obtained by the well-known Kramers–Kronig relation:[83]

$$\varepsilon_1(\omega) = 1 + \frac{2}{\pi} P \int_0^{\infty} \frac{\varepsilon_2(\omega')\omega'}{\omega'^2 - \omega^2 + i\eta} \mathrm{d}\omega', \qquad (5)$$

where P denotes the principle value. Based on the complex dielectric function, the absorption coefficient $\alpha(\omega)$ is given by:[84,85]

$$\alpha(\omega) = \frac{\sqrt{2}\omega}{c} \left\{ \left[\varepsilon_1^2(\omega) + \varepsilon_2^2(\omega) \right]^{1/2} - \varepsilon_1(\omega) \right\}^{\frac{1}{2}}, \qquad (6)$$

In 2D semiconductor materials, the band gap obtained by HSE06 is usually close to the real optical band gap due to the underestimation of the band gap by neglecting excitonic effects.[86] Thus, we only performed HSE06 calculations to obtain

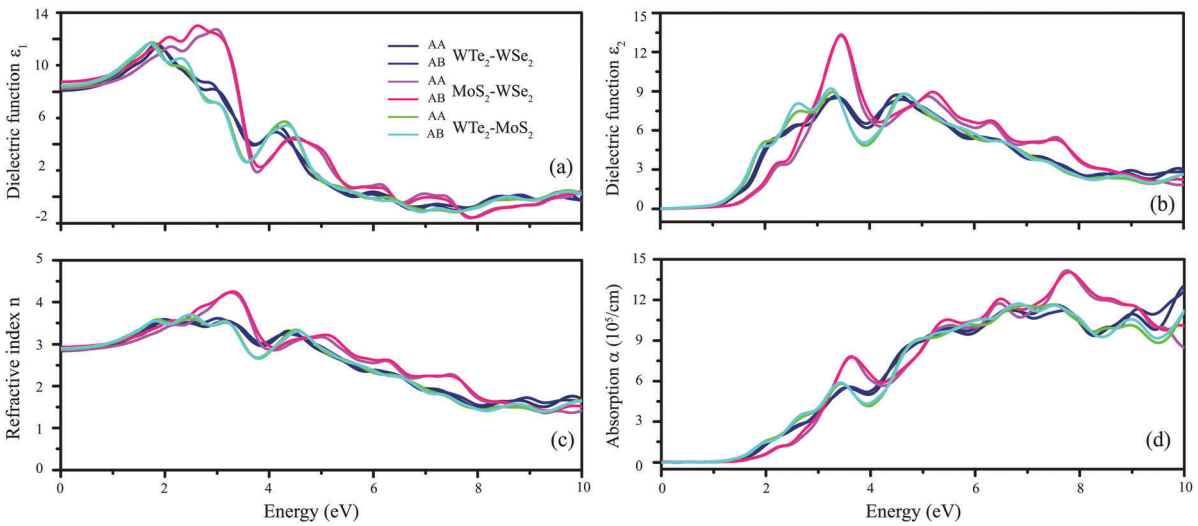

Fig. 7 HSE06 calculations of (a) the real part of the dielectric function, (b) the imaginary part of the dielectric function and (c) refractive and (d) optical absorption spectra of AA and AB stacking hetero-bilayer WTe_2–WSe_2, MoS_2–WSe_2 and WTe_2–MoS_2 for incident light with polarization along *a*.

optical properties for the hetero-bilayer MX_2 under consideration here, which show that all of them are semiconductors with a finite band gap, as shown in Table 1. All the optical constants are calculated for incident radiations with the electric field vector **E** polarized along the *a* and *b* directions,[87] as shown in Fig. 1(c).

Due to the C_3 symmetry of the hexagonal structure of the hetero-bilayer MX_2, the dielectric function $\varepsilon(\omega)$ possesses the same results along the *a* and *b* directions. The $\varepsilon(\omega)$ results for AA and AB stacking types are also close to each other, as shown in Fig. 7(a and b) and Fig. S4 (ESI†), irrespective of the corresponding Anderson band type. The similarity in $\varepsilon(\omega)$ results between AA and AB stacking hetero-bilayer MX_2 can be understood by the fact that the band structure of the hetero-bilayer MX_2 can be roughly decomposed into the respective band structures of the constituent monolayer MX_2 according to Anderson's rule. Thus, the contribution to the total optical response, *i.e.* $\varepsilon_2(\omega)$, from absorption of an incident photon $\hbar\omega$ and then transition from Ψ_k^c to Ψ_k^v, can be traced back to the behaviors of electrons located within the constituent monolayer MX_2. Therefore, the $\varepsilon_2(\omega)$ results for AA and AB stacking hetero-bilayer MX_2 probably are similar since they contain identical constituent monolayer MX_2, according to eqn (4).

The optical properties of hetero-bilayer MX_2, *e.g.* WTe_2–WSe_2, MoS_2–WSe_2 and WTe_2–MoS_2, are shown in Fig. 7. The main absorption peaks of these three hetero-bilayer MX_2 locate in the range of 3.0 to 5.0 eV, *i.e.* the ultraviolet region, with a refractive range from 2.80 to 4.27 in this region.

4 Conclusion

In this work, we have investigated the structure and electronic, mechanical, transport and optical properties of the vdW MX_2 heterostructures using first-principles calculations. The AA and AB stacked hetero-bilayer MX_2 exhibit three types of band alignment according to Anderson's rule, with a wide band gap range between 0 and 2 eV. The main differences between AA and AB stacked hetero-bilayer MX_2 lie in the band structure and mechanical properties due to the interlayer coupling, such as the indirect Γ–K band gap. The band structure of MTe_2–MX_2 will possess a higher valance band at the *M* point due to the high band energy of the $5p_{x,y}$ orbitals of Te. The type II band alignment of the vdW hetero-bilayer MX_2 makes interlayer transitions possible, leading to spatially separated excitons. The transport properties of the vdW MX_2 heterostructures are consistent with the symmetry of the geometric structures. It should be noted that the carrier mobilities of the hetero-bilayer MX_2 are often higher than those of monolayer MX_2, attributed to the higher elastic modulus for the hetero-bilayer MX_2, while the hetero-bilayer MX_2 with an indirect band gap possesses much lower hole mobilities due to the increased effective masses and deformation potential constants. Furthermore, the calculated optical properties show strong optical absorption for vdW MX_2 heterostructures, enabling novel applications in optoelectronics from the visible to ultraviolet regions, such as photodetectors, light-emitting diodes and photovoltaics.

Conflicts of interest

There are no conflicts to declare.

Acknowledgements

This work is supported by the National Natural Science Foundation of China under grant nos. 11374063 and 11404348, the National Basic Research Program of China (973 Program) under grant no. 2013CBA01505 and FDUROP (Fudan's Undergraduate Research Opportunities Program) under no. 16066. Work at Ames Laboratory is partially supported by the US Department of Energy, Office of Basic Energy Science, Division of Materials Science and Engineering (Ames Laboratory is operated for the US Department of Energy by Iowa State University under contract no. DE-AC02-07CH11358). The European Research Council under ERC Advanced grant no. 320081 (PHOTOMETA) supports work at FORTH.

References

1 K. S. Novoselov, A. K. Geim, S. V. Morozov, D. Jiang, M. I. Katsnelson, I. V. Grigorieva, S. V. Dubonos and A. A. Firsov, Two-dimensional gas of massless dirac fermions in graphene, *Nature*, 2005, **438**, 197–200.

2 H. L. Stormer, Y. Zhang, Y.-W. Tan and P. Kim, Experimental observation of the quantum hall effect and berry's phase in graphene, *Nature*, 2005, **438**(7065), 201–204.

3 C. R. Dean, A. F. Young, I. Meric, C. Lee, L. Wang, S. Sorgenfrei, K. Watanabe, T. Taniguchi, P. Kim, K. L. Shepard and J. Hone, Boron nitride substrates for high-quality graphene electronics, *Nat. Nanotechnol.*, 2010, **5**(10), 722–726.

4 M. Yankowitz, J. Xue, D. Cormode, J. D. Sanchez-Yamagishi, K. Watanabe, T. Taniguchi, P. Jarillo-Herrero, P. Jacquod and B. J. LeRoy, Emergence of superlattice dirac points in graphene on hexagonal boron nitride, *Nat. Phys.*, 2012, **8**(5), 382–386.

5 B. Radisavljevic, A. Radenovic, J. Brivio, V. Giacometti and A. Kis, Single-layer MoS_2 transistors, *Nat. Nanotechnol.*, 2011, **6**, 147–150.

6 A. Splendiani, L. Sun, Y. Zhang, T. Li, J. Kim, C.-Y. Chim, G. Galli and F. Wang, Emerging photoluminescence in monolayer MoS_2, *Nano Lett.*, 2010, **10**(4), 1271–1275.

7 D. Xiang, C. Han, J. Wu, S. Zhong, Y. Liu, J. Lin, X.-A. Zhang, W. P. Hu, B. Özyilmaz, A. H. C. Neto, A. T. Shen Wee and W. Chen, Surface transfer doping induced effective modulation on ambipolar characteristics of few-layer black phosphorus, *Nat. Commun.*, 2015, **6**, 6485.

8 L. Li, Y. Yu, G. J. Ye, Q. Ge, X. Ou, H. Wu, D. Feng, X. H. Chen and Y. Zhang, Black phosphorus field-effect transistors, *Nat. Nanotechnol.*, 2014, **9**(5), 372–377.

9 V. Tran, R. Soklaski, Y. Liang and L. Yang, Layer-controlled band gap and anisotropic excitons in few-layer black phosphorus, *Phys. Rev. B: Condens. Matter Mater. Phys.*, 2014, **89**(23), 235319.

10 M. Bernardi, M. Palummo and J. C. Grossman, Extraordinary sunlight absorption and one nanometer thick

photovoltaics using two-dimensional monolayer materials, *Nano Lett.*, 2013, **13**(8), 3664–3670.
11 D. Hennig and C. Mulhern, Collective transport of coupled particles, *Eur. Phys. J. B*, 2012, **85**(1), 1.
12 W. Zhang, Z. Huang, W. Zhang and Y. Li, Two-dimensional semiconductors with possible high room temperature mobility, *Nano Res.*, 2014, **7**(12), 1731–1737.
13 T. Cao, G. Wang, W. Han, H. Ye, C. Zhu, J. Shi, Q. Niu, P. Tan, E. Wang, B. Liu and J. Feng, Valley-selective circular dichroism of monolayer molybdenum disulphide, *Nat. Commun.*, 2012, **3**(6), 887.
14 H. Zeng, J. Dai, W. Yao, D. Xiao and X. Cui, Valley polarization in MoS_2 monolayers by optical pumping, *Nat. Nanotechnol.*, 2012, **7**(8), 490–493.
15 F. A. Rasmussen and K. S. Thygesen, Computational 2d materials database: electronic structure of transition-metal dichalcogenides and oxides, *J. Phys. Chem. C*, 2015, **119**(23), 13169–13183.
16 H. J. Conley, B. Wang, J. I. Ziegler, R. F. Haglund, S. T. Pantelides and K. I. Bolotin, Bandgap engineering of strained monolayer and bilayer MoS_2, *Nano Lett.*, 2013, **13**(8), 3626–3630.
17 K. F. Mak, C. Lee, J. Hone, J. Shan and T. F. Heinz, Atomically thin MoS_2: a new direct-gap semiconductor, *Phys. Rev. Lett.*, 2010, **105**, 136805.
18 T. G. Pedersen, C. Flindt, J. Pedersen, N. A. Mortensen, A.-P. Jauho and K. Pedersen, Graphene antidot lattices: designed defects and spin qubits, *Phys. Rev. Lett.*, 2008, **100**(13), 136804.
19 Q. Liu, L. Li, Y. Li, Z. Gao, Z. Chen and J. Lu, Tuning electronic structure of bilayer MoS_2 by vertical electric field: a first-principles investigation, *J. Phys. Chem. C*, 2012, **116**(40), 21556–21562.
20 K. S. Novoselov, A. Mishchenko, A. Carvalho and A. H. Castro Neto, 2d materials and van der Waals heterostructures, *Science*, 2016, **353**(6298), aac9439.
21 S. J. Haigh, A. Gholinia, R. Jalil, S. Romani, L. Britnell, D. C. Elias, K. S. Novoselov, L. A. Ponomarenko, A. K. Geim and R. Gorbachev, Cross-sectional imaging of individual layers and buried interfaces of graphene-based heterostructures and superlattices, *Nat. Mater.*, 2012, **11**(9), 764–767.
22 W.-T. Hsu, Z.-A. Zhao, L.-J. Li, C.-H. Chen, M.-H. Chiu, P.-S. Chang, Y.-C. Chou and W.-H. Chang, Second harmonic generation from artificially stacked transition metal dichalcogenide twisted bilayers, *ACS Nano*, 2014, **8**(3), 2951–2958.
23 W. Zhang, Q. Wang, Y. Chen, Z. Wang and A. T. S. Wee, Van der Waals stacked 2d layered materials for optoelectronics, *2D Mater.*, 2016, **3**(2), 022001.
24 H. Terrones, F. López-Urías and M. Terrones, Novel heterolayered materials with tunable direct band gaps by sandwiching different metal disulfides and diselenides, *Sci. Rep.*, 2013, **3**(3), 1549.
25 A. Kogar, M. S. Rak, S. Vig, A. A. Husain, F. Flicker, Y. I. Joe, L. Venema, G. J. MacDougall, T. C. Chiang, E. Fradkin, J. van Wezel and P. Abbamonte, Signatures of exciton condensation in a transition metal dichalcogenide, *Science*, 2017, **358**(6368), 1314–1317.
26 P. Rivera, J. R. Schaibley, A. M. Jones, J. S. Ross, S. Wu, G. Aivazian, P. Klement, K. Seyler, G. Clark, N. J. Ghimire, J. Yan, D. G. Mandrus, W. Yao and X. Xu, Observation of long-lived interlayer excitons in monolayer $MoSe_2$–WSe_2 heterostructures, *Nat. Commun.*, 2015, **6**, 6242.
27 M.-H. Chiu, C. Zhang, H.-W. Shiu, C.-P. Chuu, C.-H. Chen, C.-Y. S. Chang, C.-H. Chen, M.-Y. Chou, C.-K. Shih and L.-J. Li, Determination of band alignment in the single-layer MoS_2/WSe_2 heterojunction, *Nat. Commun.*, 2015, **6**, 7666.
28 H. Fang, C. Battaglia, C. Carraro, S. Nemsak, B. Ozdol, J. S. Kang, H. A. Bechtel, S. B. Desai, F. Kronast, A. A. Unal, G. Conti, C. Conlon, G. K. Palsson, M. C. Martin, A. M. Minor, C. S. Fadley, E. Yablonovitch, R. Maboudian and A. Javey, Strong interlayer coupling in van der Waals heterostructures built from single-layer chalcogenides, *Proc. Natl. Acad. Sci. U. S. A.*, 2014, **111**(17), 6198–6202.
29 X. Hong, J. Kim, S.-F. Shi, Y. Zhang, C. Jin, Y. Sun, S. Tongay, J. Wu, Y. Zhang and F. Wang, Ultrafast charge transfer in atomically thin MoS_2/WS2 heterostructures, *Nat. Nanotechnol.*, 2014, **9**(9), 682–686.
30 H. Heo, J. H. Sung, S. Cha, B.-G. Jang, J.-Y. Kim, G. Jin, D. Lee, J.-H. Ahn, M.-J. Lee, J. H. Shim, H. Choi and M.-H. Jo, Interlayer orientation-dependent light absorption and emission in monolayer semiconductor stacks, *Nat. Commun.*, 2015, **6**(5), 7372.
31 Y. Balaji, Q. Smets, C. J. Lockhart De La Rosa, A. K. Augustin Lu, D. Chiappe, T. Agarwal, D. H. C. Lin, C. Huyghebaert, I. Radu, D. Mocuta and G. Groeseneken, Tunneling transistors based on MoS_2/$MoTe_2$ van der Waals heterostructures, *IEEE J. Electron Devices Soc.*, 2018, **6**, 1048–1055.
32 Y. Chen, X. Wang, G. Wu, Z. Wang, H. Fang, T. Lin, S. Sun, H. Shen, W. Hu, J. Wang, J. Sun, X. Meng and J. Chu, High-performance photovoltaic detector based on MoTe2/MoS_2 van der Waals heterostructure, *Small*, 2018, **14**(9), 1703293.
33 N. Lu, H. Guo, L. Li, J. Dai, L. Wang, W.-N. Mei, X. Wu and X. C. Zeng, MoS_2/MX2 heterobilayers: bandgap engineering via tensile strain or external electrical field, *Nanoscale*, 2014, **6**(5), 2879–2886.
34 J. Kang, S. Tongay, J. Zhou, J. Li and J. Wu, Band offsets and heterostructures of two-dimensional semiconductors, *Appl. Phys. Lett.*, 2013, **102**(1), 012111.
35 G. Kresse and J. Furthmüller, Efficient iterative schemes for *ab initio* total-energy calculations using a plane-wave basis set, *Phys. Rev. B: Condens. Matter Mater. Phys.*, 1996, **54**, 11169–11186.
36 J. P. Perdew, K. Burke and M. Ernzerhof, Generalized gradient approximation made simple, *Phys. Rev. Lett.*, 1996, **77**, 3865–3868.
37 S. Grimme, Semiempirical gga-type density functional constructed with a long-range dispersion correction, *J. Comput. Chem.*, 2006, **27**(15), 1787–1799.
38 S. Grimme, J. Antony, S. Ehrlich and H. Krieg, A consistent and accurate ab initio parametrization of density functional dispersion correction (DFT-d) for the 94 elements h-pu, *J. Chem. Phys.*, 2010, **132**(15), 154104.
39 S. Grimme, S. Ehrlich and L. Goerigk, Effect of the damping function in dispersion corrected density functional theory, *J. Comput. Chem.*, 2011, **32**(7), 1456–1465.

40 J. Heyd, G. E. Scuseria and M. Ernzerhof, Hybrid functionals based on a screened coulomb potential, *J. Chem. Phys.*, 2003, **118**(18), 8207–8215.
41 J. Heyd, G. E. Scuseria and M. Ernzerhof, Erratum: Hybrid functionals based on a screened coulomb potential?, *J. Chem. Phys.*, 2003, **118**, 8207 (*J. Chem. Phys.*, 2006, **124**, 219906).
42 L. Tang, M. Q. Long, D. Wang and Z. G. Shuai, The role of acoustic phonon scattering in charge transport in organic semiconductors: a first-principles deformation-potential study, *Sci. China, Ser. B: Chem.*, 2009, **52**(10), 1646–1652.
43 Y. Cai, G. Zhang and Y. W. Zhang, Polarity-reversed robust carrier mobility in monolayer MoS_2 nanoribbons, *J. Am. Chem. Soc.*, 2014, **136**, 6269–6275.
44 M. Long, L. Tang, D. Wang, Y. Li and Z. Shuai, Electronic structure and carrier mobility in graphdiyne sheet and nanoribbons: theoretical predictions, *ACS Nano*, 2011, **5**(4), 2593–2600.
45 J. Chen, J. Xi, D. Wang and Z. Shuai, Carrier mobility in graphyne should be even larger than that in graphene: a theoretical prediction, *J. Phys. Chem. Lett.*, 2013, **4**, 1443–1448.
46 W. Yanli and Y. Ding, Electronic structure and carrier mobilities of arsenene and antimonene nanoribbons: a first-principle study, *Nanoscale Res. Lett.*, 2015, **10**, 254.
47 J. Bardeen and W. Shockley, Deformation potentials and mobilities in non-polar crystals, *Phys. Rev.*, 1950, **80**, 72–80.
48 W. Walukiewicz, H. E. Ruda, J. Lagowski and H. C. Gatos, Electron mobility in modulation-doped heterostructures, *Phys. Rev. B: Condens. Matter Mater. Phys.*, 1984, **30**(8), 4571–4582.
49 S ichi Takagi, J. L. Hoyt, J. J. Welser and J. F. Gibbons, Comparative study of phonon-limited mobility of two-dimensional electrons in strained and unstrained si metal–oxide–semiconductor field-effect transistors, *J. Appl. Phys.*, 1996, **80**(3), 1567–1577.
50 J. A. Wilson and A. D. Yoffe, The transition metal dichalcogenides discussion and interpretation of the observed optical, electrical and structural properties, *Adv. Phys.*, 1969, **18**(73), 193–335.
51 G. R. Bhimanapati, Z. Lin, V. Meunier, Y. Jung, J. Cha, S. Das, D. Xiao, Y. Son, M. S. Strano, V. R. Cooper, L. Liang, S. G. Louie, E. Ringe, W. Zhou, S. S. Kim, R. R. Naik, B. G. Sumpter, H. Terrones, F. Xia, Y. Wang, J. Zhu, D. Akinwande, N. Alem, J. A. Schuller, R. E. Schaak, M. Terrones and J. A. Robinson, Recent Advances in Two-Dimensional Materials beyond Graphene, *ACS Nano*, 2015, **9**(12), 11509–11539.
52 H. Shu, Y. Li, X. Niu and J. Wang, The stacking dependent electronic structure and optical properties of bilayer black phosphorus, *Phys. Chem. Chem. Phys.*, 2016, **18**(8), 6085–6091.
53 K. Liu, L. Zhang, T. Cao, C. Jin, D. Qiu, Q. Zhou, A. Zettl, P. Yang, S. G. Louie and F. Wang, Evolution of interlayer coupling in twisted molybdenum disulfide bilayers, *Nat. Commun.*, 2014, **5**, 4966.
54 J. L. Birman and G. Burns, *Introduction to Group Theory with Applications*, Academic Press, 1977.
55 J. H. Rose, J. Ferrante and J. R. Smith, Universal binding energy curves for metals and bimetallic interfaces, *Phys. Rev. Lett.*, 1981, **47**(9), 675–678.
56 J. Zhao, Y. Li and J. Ma, Quantum spin hall insulators in functionalized arsenene (asx, x = f, oh andch3) monolayers with pronounced light absorption, *Nanoscale*, 2016, **8**, 9657–9666.
57 S. Gao, L. Yang and C. D. Spataru, Interlayer coupling and gate-tunable excitons in transition metal dichalcogenide heterostructures, *Nano Lett.*, 2017, **17**(12), 7809–7813.
58 Z. Ji, H. Hong, J. Zhang, Q. Zhang, W. Huang, T. Cao, R. Qiao, C. Liu, J. Liang, C. Jin, L. Jiao, K. Shi, S. Meng and K. Liu, Robust stacking-independent ultrafast charge transfer in MoS_2/WS2 bilayers, *ACS Nano*, 2017, **11**(12), 12020–12026.
59 B. Amin, N. Singh and U. Schwingenschlæžšgl, Heterostructures of transition metal dichalcogenides, *Phys. Rev. B: Condens. Matter Mater. Phys.*, 2015, **92**(7), 075439.
60 Z. Zheng, X. Wang and W. Mi, Strain and electric-field tunable valley states in 2d van der Waals $MoTe_2$/WTe_2 heterostructures, *J. Phys.: Condens. Matter*, 2016, **28**(50), 505003.
61 B. Amin, T. P. Kaloni, G. Schreckenbach and M. S. Freund, Materials properties of out-of-plane heterostructures of MoS_2–WSe_2 and WS_2–$MoSe_2$, *Appl. Phys. Lett.*, 2016, **108**(6), 063105.
62 N. Lu, H. Guo, L. Li, J. Dai, L. Wang, W.-N. Mei, X. Wu and X. C. Zeng, MoS_2/MX_2 heterobilayers: bandgap engineering via tensile strain or external electrical field, *Nanoscale*, 2014, **6**(5), 2879–2886.
63 H. Jiang, Electronic band structures of molybdenum and tungsten dichalcogenides by the GW approach, *J. Phys. Chem. C*, 2012, **116**(14), 7664–7671.
64 Y. Ding, Y. Wang, J. Ni, L. Shi, S. Shi and W. Tang, First principles study of structural, vibrational and electronic properties of graphene-like MX2 (m = mo, nb, w, ta; x = s, se, te) monolayers, *Phys. B*, 2011, **406**(11), 2254–2260.
65 K. Kośmider and J. Fernández-Rossier, Electronic properties of the MoS_2–WS_2 heterojunction, *Phys. Rev. B: Condens. Matter Mater. Phys.*, 2012, **87**(7), 216.
66 W. G. Zeier, A. Zevalkink, Z. M. Gibbs, G. Hautier, M. G. Kanatzidis and G. Jeffrey Snyder, Thinking like a chemist: intuition in thermoelectric materials, *Angew. Chem., Int. Ed.*, 2016, **55**(24), 6826–6841.
67 R. L. Anderson, Germanium–gallium arsenide heterojunctions [letter to the editor], *IBM J. Res. Dev.*, 1960, **4**(3), 283–287.
68 N. Vol, What is what in the nanoworld: a handbook on nanoscience and nanotechnology, *Materials Today*, 2004, **7**(12), 49.
69 H. Fang, C. Battaglia, C. Carraro, S. Nemsak, B. Ozdol, J. S. Kang, H. A. Bechtel, S. B. Desai, F. Kronast, A. A. Unal, G. Conti, C. Conlon, G. K. Palsson, M. C. Martin, A. M. Minor, C. S. Fadley, E. Yablonovitch, R. Maboudian and A. Javey, Strong interlayer coupling in van der Waals heterostructures built from single-layer chalcogenides, *Proc. Natl. Acad. Sci. U. S. A.*, 2014, **111**(17), 6198–6202.
70 S. Zhang, M. Xie, F. Li, Z. Yan, Y. Li, E. Kan, W. Liu, Z. Chen and H. Zeng, Semiconducting group 15 monolayers: a broad range of band gaps and high carrier mobilities, *Angew. Chem., Int. Ed.*, 2016, **55**(5), 1666–1669.

71 M.-H. Chiu, C. Zhang, H.-W. Shiu, C.-P. Chuu, C.-H. Chen, C.-Y. S. Chang, C.-H. Chen, M.-Y. Chou, C.-K. Shih and L.-J. Li, Determination of band alignment in the single-layer MoS_2/WSe_2 heterojunction, *Nat. Commun.*, 2015, **6**, 7666.
72 B. Peng, H. Zhang, H. Shao, K. Xu, G. Ni, J. Li, H. Zhu and C. M. Soukoulis, Chemical intuition for high thermoelectric performance in monolayer black phosphorus, alpha-arsenene and aw-antimonene, *J. Mater. Chem. A*, 2018, **6**(5), 2018–2033.
73 S. Froyen and W. A. Harrison, Elementary prediction of linear combination of atomic orbitals matrix elements, *Phys. Rev. B: Condens. Matter Mater. Phys.*, 1979, **20**, 2420–2422.
74 A. T. Hanbicki, H.-J. Chuang, M. R. Rosenberger, C. S. Hellberg, S. V. Sivaram, K. M. McCreary, I. I. Mazin and B. T. Jonker, Double indirect interlayer exciton in a $MoSe_2/WSe_2$ van der Waals heterostructure, *ACS Nano*, 2018, **12**(5), 4719–4726.
75 J. Kang, J. Li, S.-S. Li, J.-B. Xia and L.-W. Wang, Electronic structural moiré pattern effects on $MoS_2/MoSe_2$ 2d heterostructures, *Nano Lett.*, 2013, **13**(11), 5485–5490.
76 M. Félix and F.-X. Coudert, Necessary and sufficient elastic stability conditions in various crystal systems, *Phys. Rev. B: Condens. Matter Mater. Phys.*, 2014, **90**(22), 224104.
77 B. Peng, H. Zhang, H. Shao, Z. Ning, Y. Xu, G. Ni, H. Lu, D. W. Zhang and H. Zhu, Stability and strength of atomically thin borophene from first principles calculations, *Mater. Res. Lett.*, 2017, **5**(6), 399–407.
78 R. C. Andrew, R. E. Mapasha, A. M. Ukpong and N. Chetty, Mechanical properties of graphene and boronitrene, *Phys. Rev. B: Condens. Matter Mater. Phys.*, 2012, **85**(12), 777–782.
79 F. Zeng, W.-B. Zhang and B.-Y. Tang, Electronic structures and elastic properties of monolayer and bilayer transition metal dichalcogenides MX2 (m = mo, w; x = o, s, se, te): a comparative first-principles study, *Chin. Phys. B*, 2015, **24**(9), 097103.
80 L. Yu, Q. Yan and A. Ruzsinszky, Negative poisson's ratio in 1t-type crystalline two-dimensional transition metal dichalcogenides, *Nat. Commun.*, 2017, **8**, 15224.
81 M. Gajdoš, K. Hummer, G. Kresse, J. Furthmüller and F. Bechstedt, Linear optical properties in the projector-augmented wave methodology, *Phys. Rev. B: Condens. Matter Mater. Phys.*, 2006, **73**, 045112.
82 Y. Xu, B. Peng, H. Zhang, H. Shao, R. Zhang and H. Zhu, First-principle calculations of optical properties of monolayer arsenene and antimonene allotropes, *Ann. Phys.*, 2017, 1600152.
83 M. S. Dresselhaus. *Solid State Physics Part II Optical Properties of Solids*, Citeseer, 1999.
84 S. Saha, T. P. Sinha and A. Mookerjee, Electronic structure, chemical bonding, and optical properties of paraelectric $batio_3$, *Phys. Rev. B: Condens. Matter Mater. Phys.*, 2000, **62**, 8828–8834.
85 B. Luo, X. Wang, E. Tian, G. Li and L. Li, Electronic structure, optical and dielectric properties of $batio_3/catio_3/srtio_3$ ferroelectric superlattices from first-principles calculations, *J. Mater. Chem. C*, 2015, **3**, 8625–8633.
86 J.-H. Yang, Y. Zhang, W.-J. Yin, X. G. Gong, B. I. Yakobson and S.-H. Wei, Two-dimensional sis layers with promising electronic and optoelectronic properties: theoretical prediction, *Nano Lett.*, 2016, **16**(2), 1110–1117.
87 Y. Xu, H. Zhang, H. Shao, G. Ni, J. Li, H. Lu, R. Zhang, B. Peng, Y. Zhu, H. Zhu and C. M. Soukoulis, First-principles study on the electronic, optical, and transport properties of monolayer alpha- and beta-GeSe, *Phys. Rev. B*, 2017, **96**, 245421.

